

Imaging cross-degree-of-freedom structures in biphoton spatial-polarization hyperentanglement

CHENG LI,^{1,*} GIRISH KULKARNI,^{1,†} ISAAC SOWARD,¹ YINGWEN ZHANG,^{1,2} JEREMY UPHAM,¹ DUNCAN ENGLAND,² ANDREI NOMEROTSKI,^{3,4} EBRAHIM KARIMI,^{1,2,5} AND ROBERT BOYD^{1,6,‡}

¹*Department of Physics, University of Ottawa, 25 Templeton, Ottawa, ON K1N 6N5, Canada*

²*National Research Council, 100 Sussex Dr, Ottawa, ON K1A 0R6, Canada*

³*Faculty of Nuclear Sciences and Physical Engineering, Czech Technical University, Prague 115 19, Czech Republic*

⁴*Department of Electrical and Computer Engineering, Florida International University, Miami, FL 33174, USA*

⁵*Institute for Quantum Studies, Chapman University, Orange, CA 92866, USA*

⁶*Institute of Optics, University of Rochester, Rochester, NY 14627, USA*

**cli221@uottawa.ca, †rboyd@uottawa.ca*

Abstract: Hyperentanglement, which refers to entanglement across more than one degree of freedom (DoF), is a valuable resource in photonic quantum technology. Although hyperentangled states inherently facilitate access to high-dimensional Hilbert spaces, their distinguishing feature lies in the cross-DoF structures beyond independent entanglement in each DoF, which can be leveraged to enable novel and robust information processing schemes. In particular, for a spatial-polarization hyperentangled state generated from spontaneous parametric down-conversion, the resulting polarization entanglement is structured by the spatial distribution of all interacting optical fields. Characterizing such cross-DoF structures is a crucial step towards employing hyperentangled states for practical quantum applications. Here, by performing polarization state tomography on all spatially correlated photon pairs, we have, for the first time, resolved the full-field spatial-polarization structure in a 251-dimensional hyperentangled biphoton state. We observe an entire class of near-maximally polarization-entangled states with an average concurrence of 0.8303 ± 0.0004 , characterized by biphoton polarization phases that exhibit radial and linear gradients induced by the transverse momenta of the down-converted photons and the pump beam, respectively. Our study lays important groundwork for further exploiting the high dimensionality and cross-DoF correlations in hyperentangled states for future quantum technologies.

© 2025 Optica Publishing Group

1. Introduction

Hyperentanglement, which refers to the simultaneous entanglement in multiple degrees of freedom (DoFs) [1, 2], could be a key enabler of robust quantum information technologies and advance the research in fundamental aspects of quantum physics. One important reason is its inherent advantage in achieving high dimensionality. The tensor product postulate of quantum theory implies that the resulting dimensionality of a state equals the product of the dimensionalities in each constituent DoF. The benefit of harnessing hyperentanglement is particularly prominent in photonic quantum systems: while the dimensionality of polarization entanglement is inherently limited to two, and experimental factors constrain that of the spatial entanglement, the presence of spatial-polarization hyperentanglement can effectively double the dimension-

[†]Current address: Department of Physics, Indian Institute of Technology Ropar, Rupnagar, Punjab 140001, India.

ability from what is achievable without it. The resulting high dimensionality can thus lead to tremendous potential for quantum information processing [3, 4]: it could boost security and noise-resilience in quantum communication channels [5–9], enable efficient implementations of quantum computation [10–12], improve sensitivity in metrology protocols [13, 14], and enhance noise tolerance in experimental tests on foundations of quantum theory [15, 16]. In particular, hyperentangled photons have been implemented to enable superdense coding and teleportation [17–19], enhance the noise resilience of quantum illumination [20], and improve the secure key rates of quantum communication [21–23].

The implications of using hyperentangled states extend beyond multiplying entanglement dimensionalities in different DoFs. For instance, it was shown that quantum correlations across spatial and polarization DoFs can enable novel and more robust information encoding schemes and demonstrate topological resilience against environmental noise [24]. The spatially varying polarization correlations in a hyperentangled state can also be harnessed to enable quantum holographic imaging [25] or engineer photonic cluster states for efficient quantum computation [26], implying the potential of harnessing the interplay between different DoFs for novel quantum information technologies. From a fundamental perspective, studies have shown that spatial modes of the pump beam can influence the polarization entanglement produced from spontaneous parametric down-conversion (SPDC) [27, 28], indicating the opportunity of directly generating desired cross-DoF structures in a hyperentangled state, or encoding phase images in the biphoton correlations [29] by shaping the pump beam.

Although a hyperentangled biphoton state can be readily generated from SPDC using a paired crystal configuration [1, 30], its potential, especially that embedded in the spatial-polarization structure, remains underexplored. The first and foremost reason is that the multiplicative increase in dimensionality poses a significant challenge to the efficiency of hyperentanglement characterization. For instance, a full state tomography for a bipartite state with local dimensionality d in a single DoF requires $O(d^4)$ single-outcome projective measurements [4, 31, 32]. The need to address correlations across multiple DoFs simultaneously only adds to the complexity of the problem. Without comprehensively resolving the polarization entanglement produced in each spatiotemporal mode, the rich structure produced by cross-DoF interplay reduces to a mixture of distinguishable states. As a result, the full potential of hyperentanglement becomes inaccessible, limiting its application in practical quantum devices. For instance, the work by Li et al. [27] indicates that even though each spatial mode in a multimode pump beam can generate maximum polarization entanglement through SPDC, detecting the biphotons without resolving individual spatial modes can make the entanglement appear deteriorated.

Recently, several studies have employed Tpx3Cam, a data-driven camera capable of time-stamping single photons [33–35], to enable rapid characterization of photonic entangled states produced from SPDC [36–38]. However, Ref. [36, 37] have focused only on the polarization DoF or the spatial DoF, respectively, while their photon pair sources are capable of producing hyperentangled states. As a result, the potential of hyperentanglement and the embedded cross-DoF structures has not been addressed. Furthermore, the entangled states produced in Ref. [36, 38] are first spatially postselected using single-mode fibers or polarization-maintaining fibers before being imaged onto the Tpx3Cam. Doing so effectively reduces the spatial dimensionality and obscures any cross-DoF structures imposed by the generation process. Understanding how different DoFs become interlinked is essential for tailoring hyperentangled states to specific applications. Therefore, a quantitative and comprehensive characterization of these cross-DoF structures is crucial to fully harness the potential of hyperentanglement.

In this work, we employ Tpx3Cam to comprehensively characterize the spatial-polarization structure in a hyperentangled biphoton state produced from SPDC. We first certify spatial-polarization hyperentanglement by measuring the entanglement in each constituent DoF. Measurements of position and momentum correlations estimate a Schmidt number in the spatial DoF

to be approximately 148. Spatially-resolved polarization state tomography further confirms the generation of near-maximally polarization-entangled states across the entire spatial profile of the SPDC field, with an average concurrence of 0.8303 ± 0.0004 , certifying a total hyperentanglement dimensionality of 251. To the best of our knowledge, this is the highest hyperentanglement dimensionality certified thus far. To illustrate the spatial-polarization structure in the hyperentangled state, we present the first complete spatial map of the polarization state generated from SPDC, revealing how polarization entanglement depends on the transverse momenta of the down-converted photons throughout the entire spatial profile of the SPDC field. Moreover, using a weakly focused pump beam, we experimentally characterize, for the first time, the dependence of polarization entanglement on the angular spectrum of the pump beam. Our results advance the fundamental understanding of cross-DoF structures in hyperentangled states, paving the way for novel applications in high-dimensional quantum information processing.

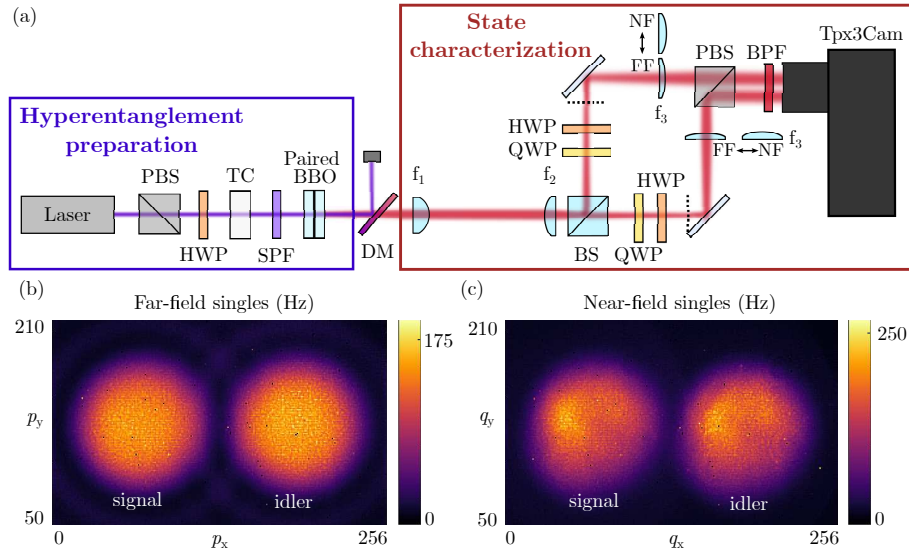


Fig. 1. (a) Schematic of the experimental setup. The β -barium borate (BBO) double-crystal produces a spatial-polarization hyperentangled state. The Tpx3Cam captures the biphoton field in the momentum or position basis through different lens configurations and in different polarization bases through combinations of the quarter-wave plate (QWP), half-wave plate (HWP), and polarizing beam splitter (PBS). TC: temporal compensator, SPF: short-pass filter with cutoff wavelength at 500 nm, DM: dichroic mirror, BS: beam splitter, BPF: band-pass filter centered at 800 nm with a bandwidth of 40 nm. $f_1 = 50$ mm, $f_2 = 100$ mm, $f_3 = 150$ mm for far-field measurements or 75 mm for near-field measurements. Dashed lines represent the intermediate planes imaging the near-field of the crystal using f_1 and f_2 . (b-c) Time-stamp histogram of photons detected in the far-field and near-field of the crystal, representing projection onto the momentum (p) and position (q) bases of the biphoton state.

2. Experimental setup

Fig. 1(a) depicts our experimental setup. An ultraviolet continuous-wave laser emits the pump beam with a center wavelength of 405 nm, a bandwidth of 2 nm, and a power of 20 mW. The pump beam is made polarized at 45° using a polarizing beam splitter (PBS) and a half-wave plate (HWP). A 5-mm temporal compensator (TC) quartz crystal introduces a time delay between the horizontal (H-) and vertical (V-) components of the pump beam, which pre-compensates for the

temporal walk-off that the two orthogonal polarization components are expected to subsequently gather inside the BBO double-crystal [39]. The BBO crystals are each 0.5-mm-thick and identically cut for type-I phase-matching, with their optical axes oriented perpendicularly to one another [30]. A 45°-polarized photon from the pump beam can then be down-converted in either crystal with equal probability to produce a pair of H-polarized or V-polarized photons. In the experiment, we orient the double-crystal for near-collinear phase matching. The down-converted photons are separated from the pump beam using a dichroic mirror (DM), and then probabilistically split into two arms using a non-polarizing beam splitter (BS). We ignore the cases wherein both the down-converted photons exit the same port of the BS, and denote photons that are reflected as *signal* and those that are transmitted as *idler*. This beam-splitting scheme ensures that measuring correlation between the signal arm and the idler arm resolves the cross-DoF structure over the full spatial profile of the SPDC. Although the probabilistic splitting reduces the coincidence rates by 50%, it does not affect the quality of entanglement or the measured cross-DoF structure compared to those obtained with deterministic splitting, as can be seen later in Fig. 3 and Fig. 4. In the low-gain regime, the output state $|\Psi\rangle$ in the far-field can be written in the joint spatial-polarization basis as

$$|\Psi\rangle = \frac{1}{\sqrt{2}} \sum_{\mathbf{p}_s, \mathbf{p}_i} c_{\mathbf{p}_s, \mathbf{p}_i} \left[|H, \mathbf{p}_s, H, \mathbf{p}_i\rangle + e^{i\phi(\mathbf{p}_s, \mathbf{p}_i)} |V, \mathbf{p}_s, V, \mathbf{p}_i\rangle \right], \quad (1)$$

where $\mathbf{p}_{s(i)}$ represents the transverse momentum of the signal (idler) photon and $c_{\mathbf{p}_s, \mathbf{p}_i}$ are complex coefficients. The quantity $\phi(\mathbf{p}_s, \mathbf{p}_i)$ represents a phase difference between the orthogonal polarization components of the state, which is dependent on the transverse momentum of the signal and the idler photons [40]. In what follows, we refer to ϕ as the *biphoton polarization phase*.

The signal and idler photons then propagate through a quarter-wave plate (QWP) and a HWP before they are either transmitted or reflected by a PBS. The photons finally pass through a bandpass filter with a center wavelength of 800 nm and full width at half maximum (FWHM) bandwidth of 40 nm before being detected by the Tpx3Cam. To characterize the entanglement in the spatial DoF, we implement two imaging schemes for realizing measurements in the position (near-field) and momentum (far-field) bases while setting the waveplates to project both the signal and idler photons into the V-polarization basis. Using the combination of $f_1 = 50$ mm, $f_2 = 100$ mm, and $f_3 = 150$ mm lenses, the far-field of the crystal is imaged on the Tpx3Cam, thereby enabling measurements in the momentum basis. On the other hand, using $f_3 = 75$ mm images the crystal output face (near-field) onto the Tpx3Cam sensor, thereby allowing for measurements in the position basis. We acquire data in the near-field and far-field for 1 minute each using the Tpx3Cam. To characterize entanglement in the polarization DoF, we additionally acquire data for 15 different combinations of orientations of HWPs and QWPs in the far-field, each for 1 minute. Combined with the VV basis data acquired in characterizing the far-field spatial correlation, these polarization measurements allow us to reconstruct the polarization density matrices corresponding to all pairs of momentum-anticorrelated pixels through quantum state tomography and characterize polarization entanglement. The total required data acquisition time for characterizing a spatial-polarization hyperentangled state is thus $2 + 15 = 17$ minutes.

The imaging sensor in Tpx3Cam comprises a 256×256 pixel array with a pixel pitch of 55 μm . The pixels in Tpx3Cam are data-driven and individually trigger the registration of photon incidence events when the signal amplitude exceeds a predefined threshold. The camera can be single photon sensitive with the addition of an image intensifier (Photonis Cricket) and have a single photon temporal resolution of 2 ns [35]. Time-stamping for individual photons can potentially allow for more versatility in data acquisition and analysis compared to frame-based imaging devices. During data acquisition, each incident photon could hit a cluster of pixels due to being amplified by the intensifier. To correct this, we apply a centroiding algorithm that

identifies the amplitude-weighed center in each cluster as the true pixel coordinate. We use the time stamp of each centroided pixel as a reference to correct the time walk within the cluster. After centroiding and time walk correction, we apply a two-pointer technique to the sorted time stamps of signal and idler photons and identify events detected within a 10-ns time window as photon coincidences [36]. Although the time walk correction algorithm can reduce the temporal resolution to 8 ns [41, 42], it should not significantly affect the efficiency of the subsequent coincidence counting with our choice of longer time window. As a result, we obtain an average coincidence rate of approximately 2.7 Hz between two spatially correlated 3×3 -pixel regions, which have similar sizes with the correlation widths measured at the Tpx3Cam sensor plane (see supplemental document for details), and an overall coincidence rate of 3200 Hz between the full signal and idler fields. We note that although the experimentally measured coincidence rate is limited by the 8% overall photon detection efficiency of the Tpx3Cam system [41], our choice of 1-minute data acquisition time has allowed us to obtain enough counts for the relevant results to be statistically valid.

3. Results and discussions

3.1. Certifying spatial-polarization hyperentanglement

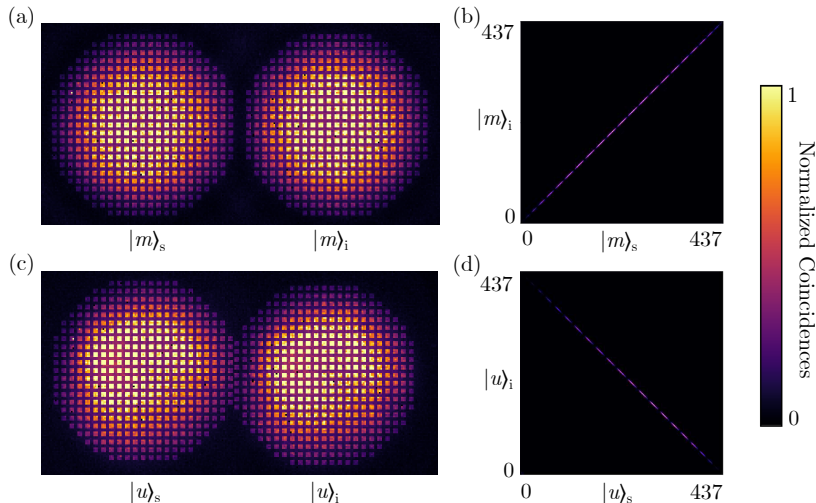


Fig. 2. Schematic depiction of (a) the discrete momentum basis in the far-field and (c) the discrete position basis in the near-field. The corresponding superpixels are depicted in a brightened color scale. Cross-correlations between the spatial modes of signal and idler photons in the (b) momentum basis and (d) position basis.

We first demonstrate the presence of hyperentanglement by certifying its high dimensionality. The dimensionality of the full spatial-polarization hyperentangled biphoton state depends primarily on the Schmidt number in the spatial DoF. While past studies have estimated this number based on certain prior assumptions about the two-photon state [43–47], some recent studies have demonstrated assumption-free protocols for certifying high dimensionality [48, 49]. In particular, it was shown that measurements in two mutually unbiased bases (MUBs) can efficiently estimate a lower bound for the Schmidt number of an entangled state, thereby certifying high-dimensional entanglement without the need for prior assumptions [48]. In our case, we show that the entanglement dimensionality in the spatial DoF can be certified by measuring the photon correlation in the discrete position basis and the discrete momentum basis, similar to the approach implemented in Ref. [50].

We denote the spatial modes of the signal(idler) photons in the discrete momentum basis as $\{|m\rangle_{s(i)}\}_{m \in [1, d]}$ and in the discrete position basis as $\{|u\rangle_{s(i)}\}_{u \in [1, d]}$. Based on the experimentally measured spatial correlation widths (see supplemental document for details), individual discrete modes in the Tpx3Cam sensor plane are better approximated by 3×3 -pixel large superpixels with 2-pixel separations between adjacent superpixels. We note that since this protocol is sensitive to noise introduced by cross-talk between non-conjugate modes, a different choice in the superpixel size and separation could lead to significant underestimation of the dimensionality. As shown in Fig. 2(a) and 2(c), we select two sets of $d = 437$ superpixels evenly distributed over the regions illuminated by signal and idler photons. The cross-correlations between spatial modes of signal and idler photons are used to calculate $\tilde{F}(\rho, \Psi)$, a lower bound for the fidelity of the experimentally measured state ρ to a maximally entangled state $|\Psi\rangle = \sum_{m=1}^d \frac{1}{\sqrt{d}} |mm\rangle$. The dimensionality of the spatial entanglement is certified to be at least $k + 1$ if k satisfies [48]

$$\tilde{F}(\rho, \Psi) > B_k(\Psi) = \sum_{m=1}^k \lambda_m^2 = \frac{k}{d}. \quad (2)$$

Upon analyzing the cross-correlations between selected spatial modes of signal and idler photons, we obtain the correlation matrices shown in Fig. 2(b) and 2(d). The fidelity lower bound is then calculated to be $\tilde{F} = 0.3383 > B_{147} = 0.3363$ (see supplemental document for details). In other words, a maximally entangled state has to have more than 147 dimensions to be transformable into our measured state through local operations and classical communication (LOCC). Therefore, the entanglement dimensionality in the spatial DoF is certified to be at least 148.

We now characterize the polarization entanglement of the biphotons produced in each spatial mode of the SPDC, thereby certifying spatial-polarization hyperentanglement. Using the setup depicted in Fig. 1(a), we perform quantum state tomography [31] using experimentally measured polarization correlation between each pair of momentum-anticorrelated (diametrically-opposite) superpixels in the far-field and reconstruct the corresponding polarization density matrix. We then compute the concurrence using $C = \max\{0, \lambda_1 - \lambda_2 - \lambda_3 - \lambda_4\}$, where λ 's are the eigenvalues of a Hermitian matrix derived from applying Pauli- y operations on reconstructed density matrices [51]. The biphoton polarization phases ϕ are computed as the phase of the $|VV\rangle \langle HH|$ elements of the reconstructed density matrices.

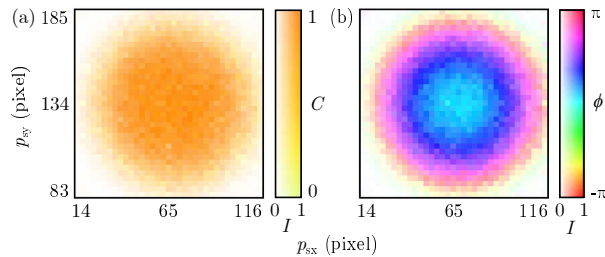


Fig. 3. (a) Concurrence C and (b) biphoton polarization phase ϕ of the biphoton states measured between momentum-correlated superpixels. The pixel coordinates correspond to the central position of the superpixels for signal photons. In the colormap, the saturation depicts the normalized pair generation rate, I , and the hue depicts C and ϕ in (a) and (b), respectively.

Fig. 3 depicts the full spatial maps of the concurrence C and biphoton polarization phase ϕ in the far field. We calculate an average concurrence of 0.8303 ± 0.0004 , which implies strong polarization entanglement with a spatially varying structure across the entire SPDC

field. Although biphoton polarization states reside in a two-dimensional Hilbert space, the effective dimensionality may be smaller for non-maximally entangled states. Therefore, it is pertinent to estimate a lower bound of the dimensionality d in the polarization DoF using the relation $\log_2 d \leq E$ [52], where E stands for the entanglement of formation [53]. For biphoton polarization states, the entanglement of formation can be derived from concurrence using [51]

$$E(C) = h\left(\frac{1 + \sqrt{1 - C^2}}{2}\right), \quad (3)$$

where $h(x) = -x \log_2 x - (1 - x) \log_2 (1 - x)$. The average entanglement of formation is then estimated to be 0.7626 ± 0.0003 . By multiplying the dimensionality lower bounds in spatial and polarization DoFs, we estimate the overall dimensionality of the hyperentangled state to be $148 \times 2^E \approx 251$.

The above result is likely to still be an underestimation of the actual dimensionality since the dimensionality certification protocol has limited resilience against the cross-talk noise [4, 48, 49]. Nevertheless, it is, to the best of our knowledge, the highest dimensionality ever certified for such an entanglement source. Moreover, the varying phase pattern displayed in Fig. 3(b) hints at a sophisticated yet potentially underexplored structure embedded in the high-dimensionality across spatial and polarization DoFs. We note that if one does not resolve the polarization entanglement at each momentum-anticorrelated photon pair, and instead mixes all pairs at a single-pixel detector, the measurements can only reconstruct a lower overall polarization entanglement. Although one can preserve entanglement after mixing by compensating for the phase differences between different pairs, we believe it is more important to understand the cross-DoF structures imposed by the generation process itself, prior to any external engineering, such as spatial compensation.

3.2. Cross-influence between spatial and polarization DoF in SPDC

Mapping the full spatial distribution of polarization entanglement is crucial for exploiting the interplay between spatial and polarization degrees of freedom in SPDC. For instance, having two distinct polarization-entangled states in different biphoton spatial modes allows the creation of photonic cluster states, which is crucial for enabling efficient quantum computation [26, 54].

The cross-influence between spatial and polarization DoFs in SPDC has two important aspects. First, the exact form of polarization entanglement depends on the transverse momenta of the *down-converted photons*. As shown in Fig. 3(b), the biphoton polarization phase ϕ displays a gradient along the radial direction, indicating polarization entanglement that varies with transverse momentum due to spatial walk-off. This effect occurs because down-converted photons emitted with different transverse momenta experience angle-dependent refractive indices inside the birefringent nonlinear medium and consequently accumulate different phase retardations between orthogonal polarization components. Consequently, a class of highly entangled states of the form of Eq. (1) with spatially varying ϕ are generated across the spatial profile of the field. While the spatial profile of polarization entanglement in SPDC has been studied for limited spatial regions or specific sets of spatial modes [1, 40], our results presenting the first full spatial distribution of polarization entanglement in the entire spatial profile of the field, laying the foundation for the controlled generation of desired hyperentangled states.

Phase-matching of the crystal also controls the relation between two-photon transverse momenta and the two-photon polarization phase. As may be noted from Fig. 3(b), the biphoton polarization phase ϕ does not vary over the full range of $-\pi$ to π in the present configuration as a consequence of the near-collinear phase matching condition. In what follows, we shall modify the experimental setup to show that by tuning the crystal orientation, an altered phase matching condition leads to ϕ varying over the full parameter space in the spatial profile of the field, which allows access to a much wider class of polarization-entangled states.

We depict our modified setup in Fig. 4(a). In order to capture the enlarged far-field image profile in its entirety, we split the SPDC field into two half-circles using a prism mirror (PM) and again recombine the fields onto the Tpx3Cam sensor. We retain the same far-field imaging scheme, such that the two-photon correlation width remains unchanged from the earlier setup, and we again perform spatially resolved polarization state tomography using the same procedure as discussed previously. In Fig. 4(b),(c), and (d), we depict the far-field intensity Tpx3Cam image, concurrence C , and biphoton polarization phase ϕ , respectively. We again observe a strong polarization entanglement in the entire spatial extent of the field with an average concurrence of 0.8847 ± 0.0006 . We notice a marginal increase in the average concurrence compared to the result in Sec. 3.1. This is likely a result of the lower polarization cross-talk since now both signal and idler photons are detected through the transmission port of the PBS. The distribution of ϕ again displays a gradient along the radial direction, but this time with ϕ having an enlarged parameter space spanning from $-\pi$ to π . In other words, the setup produces near-maximally entangled states of Eq. (1) with all possible ϕ . Thus, our setup can be configured to supply any specific state with a desired value of ϕ by post-selecting the corresponding pair of far-field pixels and tuning the phase-matching of the crystal. Such a mechanism can enable encoding spatial mode information in polarization correlations or vice versa. Furthermore, it is also possible to structure ϕ to have any desired profile by introducing additional phase differences between H- and V-polarized down-converted photons using spatial light modulators (SLMs) to enable holographic quantum imaging [25] with much higher speed. We note that such phase structures are not limited to only manifesting in momentum space. One can observe similar effects in the near field by exploring different SPDC setup geometries. We may explore near-field phase structuring in future work.

The second important aspect of this cross-influence is between the polarization DoF of the down-converted photons and the spatial DoF of the *pump beam*. Specifically, the biphoton polarization phase $\phi(\mathbf{p}_s, \mathbf{p}_i)$ in Eqn. (1) depends on the transverse momentum of the pump beam since $\mathbf{p}_p = \mathbf{p}_s + \mathbf{p}_i$ [27]. This relation is first theoretically quantified by Li et al. [27]. Here, to experimentally characterize this influence, we introduce a broader angular spectrum in the pump beam by weakly focusing it using a lens with focal length $f_0 = 100$ mm placed before the crystal. In Fig. 5, we present the influence of the angular spectrum of the pump beam on the spatial structure of the polarization states. In Fig. 5(a) and (b), we show the far-field intensity profile of the pump and the biphoton momentum correlation profile for the cases of a collimated pump and a focused pump, respectively. In Fig. 5(b), a single superpixel for the signal photons is spatially correlated with multiple superpixels for the idler photons centered around the conjugate superpixel. In other words, after focusing, the increased angular spectrum of the pump beam substantially widens the biphoton correlation width. In Fig. 5(c) and (e), we depict the results for polarization state tomography for the case of the collimated pump. To illustrate the influence of the transverse momentum of the pump beam on the polarization entanglement of the down-converted photons, we map the concurrence and phase onto pixel coordinates of the joint momentum of signal and idler, which is essentially the transverse momentum of the pump beam \mathbf{p}_p . Here, the polarization entanglement is found in a few superpixels within the narrower correlation profile, and ϕ displays little variation within the narrow angular spectrum of the collimated pump. In Fig. 5(d) and (f), we depict the results for polarization state tomography for the case of the focused pump. The concurrence map indicates the presence of polarization entanglement in all superpixels within the widened correlation profile, with an average concurrence of 0.6930 ± 0.0034 . The decrease in concurrence upon focusing the pump likely results from lower count rates and higher statistical fluctuations in individual pixels. In contrast to Fig. 5(e), the phase map illustrates a gradient of ϕ dependent on the transverse momentum of the pump beam, which is in good agreement with the theoretical predictions in Fig. 2(a) of [27]. To the best of our knowledge, this is the first direct measurement of the

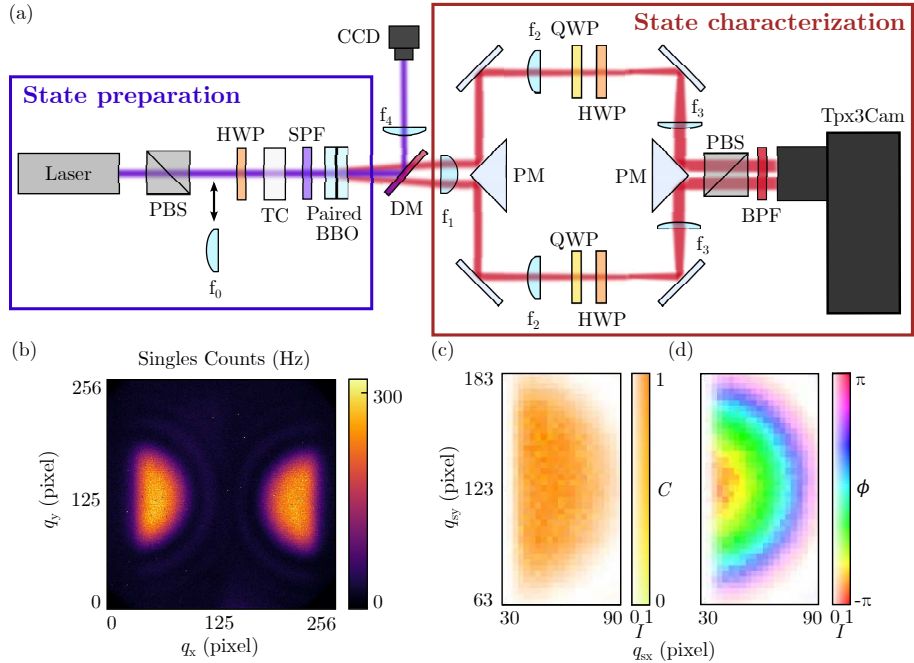


Fig. 4. (a) Schematic of the modified experimental setup. PM: prism mirror. Focal lengths of the lenses are $f_0 = 100$ mm, $f_1 = 50$ mm, $f_2 = 100$ mm, $f_3 = 150$ mm and $f_4 = 75$ mm. The angular width of the pump beam is changed by inserting f_0 into the beam path. A CCD camera images the pump beam in the Fourier plane to analyze its angular width. (b) Far-field image of the SPDC field taken by the Tpx3Cam. (c) Concurrence and (d) relative phase of the biphoton states measured between momentum-correlated superpixels. Pixel coordinates correspond to the central position of the superpixels for signal photons.

cross-influence between the spatial DoF of the pump beam and the polarization DoF of the down-converted photons. Our work opens up the opportunity to control the spatial structure of polarization states by jointly manipulating the polarization and spatial modes of the pump, which has implications in the study of topological structures of quantum light [55–57]. For instance, one can pump a paired crystal with a beam with spatially structured polarization and directly shape the correlation between spatial mode and polarization in the nonlocal optical skyrmions [24].

4. Conclusion and Outlook

In this work, we image the cross-DoF structure in spatial-polarization hyperentangled biphotons produced from SPDC using a data-driven camera capable of time-stamping single photons. We first demonstrate the rapid characterization of hyperentanglement with a cumulative measurement time of only 17 minutes. In particular, we certify the entanglement dimensionality to be about 148 in the spatial DoF using the method discussed in Refs. [48, 49]. By performing spatially-resolved polarization state tomography, we confirm the generation of an entire class of near-maximally polarization-entangled states with an average concurrence of 0.8303 ± 0.0004 in the entire spatial profile of the SPDC field, thereby certifying a spatial-polarization hyperentanglement with an estimated total dimensionality of 251. We then present the cross-influence between spatial and polarization DoF. By producing the first complete spatial map of the polar-

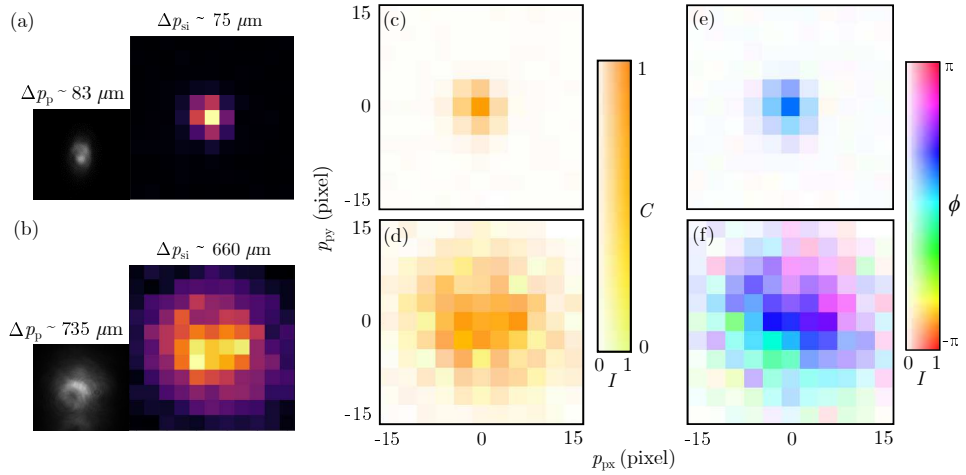


Fig. 5. Pump beam profile (greyscale image) and biphoton momentum correlation profile (colored image) for (a) collimated and (b) weakly focused pump beam. The inset captions state the beam width measured at the camera sensor plane. (c-d) Concurrence and (e-f) the biphoton polarization phase measured between a fixed signal superpixel and all momentum-correlated idler superpixels, where (c) and (e) correspond to collimated pumped beam while (d) and (f) correspond to weakly focused pump beam. Pixel coordinates indicate the transverse momenta of the pump beam $\mathbf{p}_p = \mathbf{p}_s + \mathbf{p}_i$, in which the geometrical centers of biphoton momentum correlation profile are denoted $\mathbf{p}_{px} = \mathbf{p}_{py} = 0$

ization state generated from SPDC, we illustrate the dependence of polarization entanglement on the transverse momenta of the down-converted photons in the entire spatial profile of the SPDC field. Using a weakly focused pump beam, we, for the first time, experimentally characterize the cross-influence between the polarization DoF of the down-converted photons and the spatial DoF of the pump beam.

Our results could be important for future work aimed at harnessing hyperentangled states for high-dimensional quantum information processing applications. For instance, time-stamping single photons with a data-driven camera could significantly reduce the acquisition time requirements in polarization entanglement-enabled holography [25], potentially enabling fast super-resolution imaging and microscopy [58]. Our results on cross-influence between different DoFs could extend the recent demonstration of hiding images in quantum correlations [29] to hiding and rapidly reconstructing complex phase images in spatial and polarization correlations. On the fundamental side, our work can be extended to explore the spatial-polarization cross-influence in different hyperentanglement generation schemes. For instance, it is possible to spatially resolve the polarization entanglement produced from post-selecting down-converted photons from a single Type-II nonlinear crystal [28, 59], thereby further deepening our understanding of the cross-DoF influence in SPDC. It may also be possible to build on existing work on exchange phases in Hong-Ou-Mandel interference involving high-dimensional hyperentangled photons [60] and spatially resolve such effects for a hyperentangled state. Although the current Tpx3Cam system has a low overall photon detection efficiency of 8 % [41] and is thus not yet suited for studies involving Bell-type tests of nonlocality [61], its applicability could see further expansion by implementing an image intensifier with higher quantum efficiency and higher gain. For instance, a minimum detection efficiency of 2/3 is required to close the fair-sampling loophole in Bell tests [62].

Funding. National Science Foundation (2244031); U.S. Department of Energy (76295); Natural Sciences

and Engineering Research Council of Canada (RGPIN/2017-06880); Canada First Research Excellence Fund (072623).

Acknowledgement. The authors thank X. Gao, A. D’Errico, B. Braverman, S. Karan, and M. Krenn for fruitful discussions. C. Li acknowledges P. Svihra for helpful advice on data processing.

Data availability. All relevant data are available from the corresponding author upon reasonable request.

Disclosures. The authors declare no conflict of interest.

References

1. J. T. Barreiro, N. K. Langford, N. A. Peters, and P. G. Kwiat, “Generation of hyperentangled photon pairs,” *Phys. Rev. Lett.* **95**, 260501 (2005). Publisher: American Physical Society.
2. Z. Xie, T. Zhong, S. Shrestha, *et al.*, “Harnessing high-dimensional hyperentanglement through a biphoton frequency comb,” *Nat. Photonics* **9**, 536–542 (2015).
3. M. Erhard, M. Krenn, and A. Zeilinger, “Advances in high-dimensional quantum entanglement,” *Nat. Rev. Phys.* **2**, 365–381 (2020). Number: 7 Publisher: Nature Publishing Group.
4. N. Friis, G. Vitagliano, M. Malik, and M. Huber, “Entanglement certification from theory to experiment,” *Nat. Rev. Phys.* **1**, 72–87 (2019). Number: 1 Publisher: Nature Publishing Group.
5. V. Karimipour, A. Bahraminasab, and S. Bagherinezhad, “Quantum key distribution for d -level systems with generalized bell states,” *Phys. Rev. A* **65**, 052331 (2002).
6. N. J. Cerf, M. Bourennane, A. Karlsson, and N. Gisin, “Security of quantum key distribution using d-level systems,” *Phys. Rev. Lett.* **88** (2002).
7. M. Fujiwara, M. Takeoka, J. Mizuno, and M. Sasaki, “Exceeding the classical capacity limit in a quantum optical channel,” *Phys. Rev. Lett.* **90**, 167906 (2003).
8. F. Bouchard, R. Fickler, R. W. Boyd, and E. Karimi, “High-dimensional quantum cloning and applications to quantum hacking,” *Sci. Adv.* **3**, e1601915 (2017). Publisher: American Association for the Advancement of Science.
9. S. Ecker, F. Bouchard, L. Bulla, *et al.*, “Overcoming noise in entanglement distribution,” *Phys. Rev. X* **9**, 041042 (2019).
10. T. C. Ralph, K. J. Resch, and A. Gilchrist, “Efficient toffoli gates using qudits,” *Phys. Rev. A* **75**, 022313 (2007).
11. B. P. Lanyon, M. Barbieri, M. P. Almeida, *et al.*, “Simplifying quantum logic using higher-dimensional hilbert spaces,” *Nat Phys* **5**, 134–140 (2009).
12. C. Reimer, S. Sciara, P. Roztocki, *et al.*, “High-dimensional one-way quantum processing implemented on d-level cluster states,” *Nat. Phys.* **15** (2019).
13. A. K. Jha, G. S. Agarwal, and R. W. Boyd, “Supersensitive measurement of angular displacements using entangled photons,” *Phys. Rev. A* **83**, 053829 (2011).
14. V. D’Ambrosio, N. Spagnolo, L. Del Re, *et al.*, “Photonic polarization gears for ultra-sensitive angular measurements,” *Nat. Commun.* **4**, 2432 EP – (2013).
15. D. Kaszlikowski, P. Gnacinski, M. Zukowski, *et al.*, “Violations of local realism by two entangled n-dimensional systems are stronger than for two qubits,” *Phys. Rev. Lett.* **85**, 4418–4421 (2000).
16. D. Collins, N. Gisin, N. Linden, *et al.*, “Bell inequalities for arbitrarily high-dimensional systems,” *Phys. Rev. Lett.* **88**, 040404 (2002).
17. X.-L. Wang, X.-D. Cai, Z.-E. Su, *et al.*, “Quantum teleportation of multiple degrees of freedom of a single photon,” *Nature* **518**, 516 (2015).
18. T. M. Graham, H. J. Bernstein, T.-C. Wei, *et al.*, “Superdense teleportation using hyperentangled photons,” *Nat. Commun.* **6**, 7185 (2015).
19. X.-M. Hu, Y. Guo, B.-H. Liu, *et al.*, “Beating the channel capacity limit for superdense coding with entangled ququarts,” *Sci. Adv.* **4**, eaat9304 (2018).
20. A. V. Prabhu, B. Suri, and C. M. Chandrashekar, “Hyperentanglement-enhanced quantum illumination,” *Phys. Rev. A* **103**, 052608 (2021).
21. F. Wu, G. Yang, H. Wang, *et al.*, “High-capacity quantum secure direct communication with two-photon six-qubit hyperentangled states,” *Sci. China Physics, Mech. & Astron.* **60**, 120313 (2017).
22. J.-H. Kim, Y. Kim, D.-G. Im, *et al.*, “Noise-resistant quantum communications using hyperentanglement,” *Optica* **8**, 1524–1531 (2021).
23. L. Nemirovsky-Levy, U. Pereg, and M. Segev, “Increasing quantum communication rates using hyperentangled photonic states,” *Opt. Quantum* **2**, 165–172 (2024).
24. P. Ornelas, I. Nape, R. de Mello Koch, and A. Forbes, “Non-local skyrmions as topologically resilient quantum entangled states of light,” *Nat. Photonics* **18**, 258–266 (2024).
25. H. Defienne, B. Ndagano, A. Lyons, and D. Faccio, “Polarization entanglement-enabled quantum holography,” *Nat. Phys.* **17**, 591–597 (2021). Number: 5 Publisher: Nature Publishing Group.
26. G. Vallone, G. Donati, R. Ceccarelli, and P. Mataloni, “Six-qubit two-photon hyperentangled cluster states: Characterization and application to quantum computation,” *Phys. Rev. A* **81**, 052301 (2010).

27. C. Li, B. Braverman, G. Kulkarni, and R. W. Boyd, “Experimental generation of polarization entanglement from spontaneous parametric down-conversion pumped by spatiotemporally highly incoherent light,” *Phys. Rev. A* **107**, L041701 (2023). Publisher: American Physical Society.

28. W. Zhang, D. Xu, and L. Chen, “Polarization entanglement from parametric down-conversion with an LED pump,” *Phys. Rev. Appl.* **19**, 054079 (2023). Publisher: American Physical Society.

29. C. Vernière and H. Defienne, “Hiding images in quantum correlations,” *Phys. Rev. Lett.* **133**, 093601 (2024).

30. P. G. Kwiat, E. Waks, A. G. White, *et al.*, “Ultrabright source of polarization-entangled photons,” *Phys. Rev. A* **60**, R773–R776 (1999). Publisher: American Physical Society.

31. D. F. V. James, P. G. Kwiat, W. J. Munro, and A. G. White, “Measurement of qubits,” *Phys. Rev. A* **64**, 052312 (2001). Publisher: American Physical Society.

32. N. Herrera Valencia, V. Srivastav, M. Pivoluska, *et al.*, “High-Dimensional Pixel Entanglement: Efficient Generation and Certification,” *Quantum* **4**, 376 (2020).

33. M. Fisher-Levine and A. Nomerotski, “Timepixcam: a fast optical imager with time-stamping,” *J. Instrumentation* **11**, C03016 (2016).

34. A. Nomerotski, “Imaging and time stamping of photons with nanosecond resolution in timepix based optical cameras,” *Nucl. Instruments Methods Phys. Res. Sect. A: Accel. Spectrometers, Detect. Assoc. Equip.* **937**, 26–30 (2019).

35. A. Nomerotski, M. Chekhlov, D. Dolzhenko, *et al.*, “Intensified tpx3cam, a fast data-driven optical camera with nanosecond timing resolution for single photon detection in quantum applications,” *J. Instrumentation* **18**, C01023 (2023).

36. C. Ianzano, P. Svihra, M. Flament, *et al.*, “Fast camera spatial characterization of photonic polarization entanglement,” *Sci. Reports* **10**, 6181 (2020). Number: 1 Publisher: Nature Publishing Group.

37. B. Courme, C. Vernière, P. Svihra, *et al.*, “Quantifying high-dimensional spatial entanglement with a single-photon-sensitive time-stamping camera,” *Opt. Lett.* **48**, 3439–3442 (2023). Publisher: Optica Publishing Group.

38. X. Gao, Y. Zhang, A. D’Errico, *et al.*, “Full spatial characterization of entangled structured photons,” *Phys. Rev. Lett.* **132**, 063802 (2024).

39. Y. Nambu, K. Usami, Y. Tsuda, *et al.*, “Generation of polarization-entangled photon pairs in a cascade of two type-i crystals pumped by femtosecond pulses,” *Phys. Rev. A* **66**, 033816 (2002). Publisher: American Physical Society.

40. J. B. Altepeter, E. R. Jeffrey, and P. G. Kwiat, “Phase-compensated ultra-bright source of entangled photons,” *Opt. Express* **13**, 8951–8959 (2005). Publisher: Optica Publishing Group.

41. V. Vidyapin, Y. Zhang, D. England, and B. Sussman, “Characterisation of a single photon event camera for quantum imaging,” *Sci. Reports* **13**, 1009 (2023).

42. Y. Zhang, D. England, A. Nomerotski, *et al.*, “Multidimensional quantum-enhanced target detection via spectrotemporal-correlation measurements,” *Phys. Rev. A* **101**, 053808 (2020).

43. C. K. Law and J. H. Eberly, “Analysis and interpretation of high transverse entanglement in optical parametric down conversion,” *Phys. Rev. Lett.* **92**, 127903 (2004). Publisher: American Physical Society.

44. H. Di Lorenzo Pires, C. H. Monken, and M. P. van Exter, “Direct measurement of transverse-mode entanglement in two-photon states,” *Phys. Rev. A* **80**, 022307 (2009).

45. M. P. Edgar, D. S. Tasca, F. Izdebski, *et al.*, “Imaging high-dimensional spatial entanglement with a camera,” *Nat. Commun.* **3**, 984 (2012). Number: 1 Publisher: Nature Publishing Group.

46. F. Devaux, A. Mosset, P.-A. Moreau, and E. Lantz, “Imaging spatiotemporal hong-ou-mandel interference of biphoton states of extremely high schmidt number,” *Phys. Rev. X* **10**, 031031 (2020).

47. X. Gao, Y. Zhang, A. D’Errico, *et al.*, “High-speed imaging of spatiotemporal correlations in hong-ou-mandel interference,” *Opt. Express* **30**, 19456–19464 (2022).

48. J. Bavaresco, N. Herrera Valencia, C. Klöckl, *et al.*, “Measurements in two bases are sufficient for certifying high-dimensional entanglement,” *Nat. Phys.* **14**, 1032–1037 (2018). Number: 10 Publisher: Nature Publishing Group.

49. P. Erker, M. Krenn, and M. Huber, “Quantifying high dimensional entanglement with two mutually unbiased bases,” *Quantum* **1**, 22 (2017). Publisher: Verein zur Förderung des Open Access Publizierens in den Quantenwissenschaften.

50. B. Ndagano, H. Defienne, A. Lyons, *et al.*, “Imaging and certifying high-dimensional entanglement with a single-photon avalanche diode camera,” *npj Quantum Inf.* **6**, 1–8 (2020). Number: 1 Publisher: Nature Publishing Group.

51. W. K. Wootters, “Entanglement of formation of an arbitrary state of two qubits,” *Phys. Rev. Lett.* **80**, 2245–2248 (1998). Publisher: American Physical Society.

52. M. A. Nielsen and I. L. Chuang, *Quantum Computation and Quantum Information: 10th Anniversary Edition* (Cambridge University Press, 2010).

53. W. K. Wootters, “Entanglement of formation and concurrence,” *Quantum Info. Comput.* **1**, 27–44 (2001).

54. M. Ciampini, A. Orioux, S. Paesani *et al.*, “Path-polarization hyperentangled and cluster states of photons on a chip,” *Light. Sci. & Appl.* **5**, e16064 (2016).

55. C. He, Y. Shen, and A. Forbes, “Towards higher-dimensional structured light,” *Light. Sci. & Appl.* **11**, 205 (2022). Number: 1 Publisher: Nature Publishing Group.

56. Y. Shen, Q. Zhang, P. Shi, *et al.*, “Optical skyrmions and other topological quasiparticles of light,” *Nat. Photonics* **18**, 15–25 (2024).

57. I. Nape, B. Sephton, P. Ornelas, *et al.*, “Quantum structured light in high dimensions,” *APL Photonics* **8**, 051101 (2023).
58. H. Defienne, P. Cameron, B. Ndagano, *et al.*, “Pixel super-resolution with spatially entangled photons,” *Nat. Commun.* **13**, 3566 (2022).
59. C. E. Kuklewicz, M. Fiorentino, G. Messin, *et al.*, “High-flux source of polarization-entangled photons from a periodically poled ktiopO_4 parametric down-converter,” *Phys. Rev. A* **69**, 013807 (2004).
60. Z.-F. Liu, C. Chen, J.-M. Xu, *et al.*, “Hong-ou-mandel interference between two hyperentangled photons enables observation of symmetric and antisymmetric particle exchange phases,” *Phys. Rev. Lett.* **129**, 263602 (2022).
61. C. K. Zeitler, J. C. Chapman, E. Chitambar, and P. G. Kwiat, “Entanglement verification of hyperentangled photon pairs,” *Phys. Rev. Appl.* **18**, 054025 (2022).
62. N. Gisin and B. Gisin, “A local hidden variable model of quantum correlation exploiting the detection loophole,” *Phys. Lett. A* **260**, 323–327 (1999).

Imaging cross-degree-of-freedom structures in biphoton spatial-polarization hyperentanglement: supplemental document

1. OBSERVATION OF SPATIAL ENTANGLEMENT THROUGH THE VIOLATION OF EINSTEIN-PODOLSKY-ROSEN CRITERIA

In Fig. S1, we depict the experimentally measured x - and y -components of the spatial correlation profile in both the position and momentum basis. We note the strong position correlations and momentum anti-correlations between the photons, which is a characteristic feature of spatial entanglement. Specifically, Fig. S1(c) and (f) depict the biphoton correlation profiles in the joint momentum and position coordinates of the down-converted photons. From these results, we conclude that in the Tpx3Cam sensor plane, individual discrete momentum and position modes are best approximated by 3×3 -pixel large superpixels.

The results also allow us to quantitatively verify spatial entanglement by demonstrating violations of the Einstein-Podolsky-Rosen (EPR) criteria [1, 2]. We first obtain near-field (NF) and far-field (FF) correlation widths Δ_{NF} and Δ_{FF} , respectively, at the Tpx3Cam sensor plane by fitting Gaussians to the spatial correlation profiles of Fig. S1 in the x - and y -directions [2–4]. We then calculate the position and momentum uncertainties using the relations

$$\Delta(p_{ir}|p_{sr}) = \frac{k_{si}\hbar}{f_e} \Delta_{\text{FF}}, \quad (\text{S1a})$$

$$\Delta(q_{ir}|q_{sr}) = \frac{1}{M} \Delta_{\text{NF}}, \quad (\text{S1b})$$

where $p_{sr(ir)}$ and $q_{sr(ir)}$ stand for the momentum and position of the signal (idler) photons, respectively, $r = x, y$ represent the x - and y -components of the quantities, $k_{si} = (2\pi/810) \text{ nm}^{-1}$ is the wavevector of the signal and idler photons, $f_e = 75 \text{ mm}$ is the effective focal length of our far-field imaging system and $M = 2$ is the magnification of our near-field imaging system. We summarize our results in Table 1 and compute the conditional Heisenberg uncertainty products as

$$\Delta_{\min} p_x \Delta_{\min} q_x = (0.11 \pm 0.05) \hbar < \hbar/2, \quad (\text{S2a})$$

$$\Delta_{\min} p_y \Delta_{\min} q_y = (0.12 \pm 0.03) \hbar < \hbar/2, \quad (\text{S2b})$$

which clearly violates the EPR criteria in both the x - and y -directions. We note that the asymmetry observed in the x -components of the position correlation, which is depicted in Fig. S1(d), is likely a consequence of a distortion in the pump's intensity profile. As depicted in Fig. 1(c) in the main text, the near-field singles rates display a non-Gaussian spatial profile as a result of the distorted pump profile. Although this imperfection may affect the verification of spatial entanglement using the EPR criterion, which requires the pump beam to have a Gaussian profile [4], it does not refute our conclusions regarding the certification of hyperentanglement, as our entanglement certification protocol does not rely on Gaussian approximations of the SPDC field profiles [5].

2. ESTIMATION OF FIDELITY LOWER BOUND

Following the approaches described in [6], we certify the dimensionality of entanglement in the spatial degree of freedom using correlations in two mutually unbiased bases (MUBs) [5, 7]. In Sec. 3.1 of the main text, we have defined the two MUBs to be the discrete momentum basis $\{|m\rangle_{s(i)}\}_{m \in [1,d]}$ and the discrete position basis $\{|u\rangle_{s(i)}\}_{u \in [1,d]}$.

Table S1. Measurement uncertainties inferred from spatial correlation profiles

Quantity	Values	Units
$\Delta_{\min} p_x$	$(4.9 \pm 0.2) \times 10^{-3}$	$\hbar/\mu\text{m}$
$\Delta_{\min} p_y$	$(6.4 \pm 0.3) \times 10^{-3}$	$\hbar/\mu\text{m}$
$\Delta_{\min} q_x$	18.76 ± 9.49	μm
$\Delta_{\min} q_y$	18.18 ± 3.63	μm

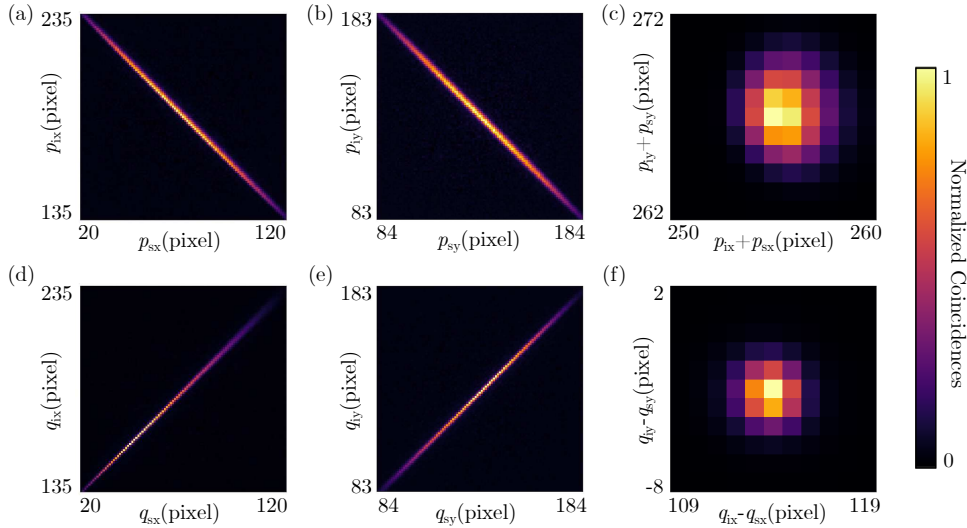


Fig. S1. Spatial correlation profiles measured in the x -components, y -components, and joint coordinates of the (a-c) momentum and (d-f) position of the signal-idler photons.

The fidelity $F(\rho, \Psi)$ of the experimentally measured state ρ to a maximally entangled state $|\Psi\rangle = \sum_{m=1}^d \frac{1}{\sqrt{d}} |mm\rangle$ is defined as:

$$\begin{aligned}
 F(\rho, \Psi) &= \text{Tr} (|\Psi\rangle \langle \Psi| \rho) \\
 &= \sum_{m,n=1}^d \langle mm| \rho |nn\rangle \\
 &= F_1(\rho, \Psi) + F_2(\rho, \Psi),
 \end{aligned} \tag{S3}$$

where

$$F_1(\rho, \Psi) = \sum_{m=1}^d \langle mm| \rho |mm\rangle, \tag{S4}$$

$$F_2(\rho, \Psi) = \sum_{m \neq n} \langle mm| \rho |nn\rangle. \tag{S5}$$

Since for an arbitrary state ρ with a Schmidt number of $k \leq d$, the fidelity satisfies

$$F(\rho, \Psi) \leq B_k(\Psi) = \frac{k}{d}, \tag{S6}$$

the entanglement dimensionality of a state with $F(\rho, \Psi) > B_k(\Psi)$ must be at least $k + 1$. As we will show in the following, correlations in the two MUBs will allow us to obtain a lower bound for the fidelity via $\tilde{F}(\rho, \Psi) = F_1(\rho, \Psi) + \tilde{F}_2(\rho, \Psi) \leq F_1(\rho, \Psi) + F_2(\rho, \Psi) = F(\rho, \Psi)$

The coincidence counts N_{mn} measured in the discrete momentum basis allow us to calculate $F_1(\rho, \Psi)$ using

$$\langle mn | \rho | mn \rangle = \frac{N_{mn}}{\sum_{k,l} N_{kl}}. \quad (S7)$$

Supplementing the coincidence counts N_{uv} measured in the discrete position basis allows us to calculate $\tilde{F}_2(\rho, \Psi)$, the lower bound of $F_2(\rho, \Psi)$, via

$$\begin{aligned} \tilde{F}_2(\rho, \Psi) &= \sum_{u=0}^{d-1} \langle uu | \rho | uu \rangle - \frac{1}{d} \\ &- \sum_{m \neq n', m \neq n, n \neq n', n' \neq m'} \gamma_{mnm'n'} \sqrt{\langle mn | \rho | mn \rangle \langle m'n' | \rho | m'n' \rangle}, \end{aligned} \quad (S8)$$

where

$$\langle uv | \rho | uv \rangle = \frac{N_{uv}}{\sum_{k,l} N_{kl}}, \quad (S9)$$

$$\gamma_{mnm'n'} = \begin{cases} 0 & \text{if } (m - m' - n + n') \bmod d \neq 0 \\ 1/d & \text{otherwise.} \end{cases} \quad (S10)$$

As a result, we calculate a lower bound of the fidelity $\tilde{F}(\rho, \Psi) = 0.3383 > B_{147} = 0.33635$, which certifies the entanglement dimensionality to be 148.

REFERENCES

1. M. D. Reid, "Demonstration of the einstein-podolsky-rosen paradox using nondegenerate parametric amplification," *Phys. Rev. A* **40**, 913–923 (1989). Publisher: American Physical Society.
2. A. Bhattacharjee, N. Meher, and A. K. Jha, "Measurement of two-photon position-momentum einstein–podolsky–rosen correlations through single-photon intensity measurements," *New J. Phys.* **24**, 053033 (2022).
3. C. H. Monken, P. H. S. Ribeiro, and S. Pádua, "Transfer of angular spectrum and image formation in spontaneous parametric down-conversion," *Phys. Rev. A* **57**, 3123–3126 (1998). Publisher: American Physical Society.
4. C. K. Law and J. H. Eberly, "Analysis and interpretation of high transverse entanglement in optical parametric down conversion," *Phys. Rev. Lett.* **92**, 127903 (2004). Publisher: American Physical Society.
5. P. Erker, M. Krenn, and M. Huber, "Quantifying high dimensional entanglement with two mutually unbiased bases," *Quantum* **1**, 22 (2017). Publisher: Verein zur Förderung des Open Access Publizierens in den Quantenwissenschaften.
6. B. Ndagano, H. Defienne, A. Lyons, *et al.*, "Imaging and certifying high-dimensional entanglement with a single-photon avalanche diode camera," *npj Quantum Inf.* **6**, 1–8 (2020). Number: 1 Publisher: Nature Publishing Group.
7. J. Bavaresco, N. Herrera Valencia, C. Klöckl, *et al.*, "Measurements in two bases are sufficient for certifying high-dimensional entanglement," *Nat. Phys.* **14**, 1032–1037 (2018). Number: 10 Publisher: Nature Publishing Group.